

X-ray Halo Around the Spiral Galaxy NGC 4631 Observed with Suzaku

Noriko Y. YAMASAKI¹, Kosuke SATO², Ikuyuki MITSUISHI¹, Takaya OHASHI³

¹*Institute of Space and Astronautical Science, Japan Aerospace Exploration Agency (ISAS/JAXA),
3-1-1 Yoshinodai, Sagami-hara, Kanagawa, 229-8510
yamasaki@astro.isas.jaxa.jp*

²*Graduate School of Natural Science and Technology, Kanazawa University, Kakuma, Kanazawa, Ishikawa, 920-1192*

³*Department of Physics, Tokyo Metropolitan University,
1-1 Minami-Osawa, Hachioji, Tokyo, 192-0397*

(Received 2008 July 30; accepted 2008 August 29)

Abstract

Suzaku observation of the edge-on spiral galaxy NGC 4631 confirmed its X-ray halo extending out to about 10 kpc from the galactic disk. The XIS spectra yielded the temperature and metal abundance for the disk and the halo regions. The observed abundance pattern for O, Ne, Mg, Si and Fe is consistent with the metal yield from type II supernovae, with an O mass of about $10^6 M_{\odot}$ contained in the halo. These features imply that metal-rich gas produced by type II supernova is brought into the halo region very effectively, most likely through a galactic wind. Temperature and metal abundance may be affected by charge exchange and dust. An upper limit for the hard X-ray flux was obtained, corresponding to a magnetic field higher than $0.5 \mu\text{G}$.

Key words: galaxies:abundances, galaxies:starburst, galaxies:halos, galaxies:individual (NGC 4631)

1. Introduction

For the understanding of the chemical evolution of galaxies and clusters of galaxies, precise knowledge about the metal production from Type Ia (SN Ia) and Type II (SN II) supernovae (SNe) is of vital importance. X-ray imaging spectroscopy of supernova remnants (SNRs), galaxies and intra-cluster medium (ICM) has shown that metal abundances generally vary from source to source. However, Sato et al. (2007a) determined the abundances of O, Ne, Mg, Si, and Fe in several galaxy clusters based on Suzaku observations, and found that the abundance patterns are commonly represented by a combination of type Ia and II supernovae products with an occurrence number ratio of 1:3.5, based on the theoretical yields from SN II and SN Ia. In order to further look into the past history of the two types of supernova, we need more precise knowledge about the metal yields from the different SNe types. It is, however, quite difficult to extract pure supernova products, in particular for the X-ray emitting hot gas. When we observe young supernova remnants (SNR), there is always a mixture of supernova ejecta and surrounding ISM and line intensities also strongly depend on the ionization condition. One way to provide a good constraint is to observe X-ray halos around starburst galaxies, which are considered to be maintained by the enhanced SNe II activity in the recent time.

Recent X-ray observations of starforming galaxies showed that metals are contained in the extended hot halo of the galaxies. For M82 and NGC 253, RGS spectra for several sliced regions along the outflow axis showed lines from highly ionized O, Ne, Mg, Si and Fe (Read & Stevens 2002; Bauer et al. 2007). The observed intensity ratios of

the lines indicates that the gas is cooling as it travels outward from the galaxy disk and that the gas around NGC 253 could be partly out of ionization equilibrium. Suzaku observations of a “cap” region of M82, which is 11.6 kpc north of the galaxy and is possibly a termination region of the hot-gas outflow, showed a spectrum consisting of emission lines from O through Fe (Tsuru et al. 2007). These spectral features strongly suggest that fresh metal-rich gas produced in the starforming region is flowing out mainly along the minor axis of galaxies. However, metal abundances in the halo gas has so far not been well-constrained. RGS data are limited in statistics, and both the EPIC and the ACIS instruments do not have sufficient energy resolution below 1 keV (e.g. Tüllmann et al. 2006). Suzaku offers a good opportunity for measuring the metallicity of the outflowing hot gas.

NGC 4631 is a nearby Sc/SBd galaxy with an edge-on morphology with the distance estimated to be about 7.5 Mpc, where $1'$ corresponds to 2.2 kpc. Estimated mass by the Tully-Fisher relation is $2.6 \times 10^{10} M_{\odot}$ (Strickland et al. 2004). The inclination and position angle are 81° and 356° respectively. This galaxy is suitable for Suzaku observations of the X-ray halo maintained by its SN activity. With its radio halo (Hummel & Dettmar 1990) and warm IR ratio, it is classified as a mild disk-wide starburst galaxy (Golla & Wielebinski 1994). An extended X-ray halo was discovered by ROSAT (Wang et al. 1995), and it has been well studied with Chandra (Wang et al. 2001; Oshima 2003; Strickland et al. 2004) and XMM-Newton (Tüllmann et al. 2006). The size of the halo is several arcmin and no X-ray counterpart for the central AGN has been detected (Strickland et al. 2004). The association of an H α filament with the X-ray emission has

been discovered (Wang et al. 2001), and FUSE also detected O VI lines from a region at $2'$ above the disk (Otte et al. 2003). These strongly suggest that a halo around NGC 4631 is the site of galactic outflow or fountain, where the gas is floating up from the disk by the SN energy input and possibly cooling.

Another important feature of the halo is the extended synchrotron radio emission, which is observed from several star-forming galaxies (e.g. Veilleux et al. 2005). These radio halos are populated with relativistic electrons together with magnetic fields of an order of $10\mu\text{G}$. The radial orientation of the magnetic field lines suggests that the field has been carried into the halo region by the outflow of hot gas (Golla & Hummel 1994). In some cases, the hot gas may be confined in the halo when the magnetic pressure exceeds the thermal pressure (Wang et al. 1995). To constrain how the non-thermal energy is distributed in the halo, it is important to look into the possibility of non-thermal emission in the hard X-ray band.

Throughout this paper we adopt the Galactic hydrogen column density of $N_{\text{H}} = 1.27 \times 10^{20} \text{ cm}^{-2}$ (Dickey & Lockman 1990) in the direction of NGC 4631. The solar abundance table is given by Anders & Grevesse (1989), and the errors are the 90% confidence limits for a single interesting parameter.

2. Observation and Data Reduction

2.1. Observation

Suzaku carried out observations of the starburst galaxy NGC 4631 in November 2006 (PI: N. Y. Yamasaki) with an exposure of 81 ks. The observation log is given in table 1. The X-ray Imaging Spectrometer (XIS: Koyama et al. 2007) instrument consists of a back-illuminated (BI: XIS 1) CCD sensor and two front-illuminated (FI: XIS 0, 3) sensors. The XIS was operated in the Normal clocking mode (8 s exposure per frame), with the standard 5×5 or 3×3 editing mode. The observed X-ray image in 0.6 – 0.7 keV band and XIS contour image in 0.5–2.0 keV range overlaid on the optical image by DSS is shown in figure 1 .

2.2. Data Reduction

We used version 2.0.6 processing data (Mitsuda et al. 2007), and the analysis was performed with HEASoft version 6.4 and XSPEC 11.3.2aj. In the analysis of XIS data, we selected $ELEVATION > 15^\circ$ of the data set to remove stray-light from the day Earth limb, and the light curve of each sensor in the 0.3–10 keV range with a 16 s time bin was also examined so as to exclude periods of an anomalous event rate greater or less than $\pm 3\sigma$ around the mean. After the above screenings, the remaining exposures of the observations decreased by $\sim 7\%$ as shown in table 1. Event screening with cut-off rigidity (COR) was not performed in our data.

In order to subtract the non X-ray background (NXB), we used a dark Earth database, provided by the “xisnxbgen” ftools task (Tawa et al. 2008). Although it is known that the optical blocking filters of the XIS have grad-

ually been contaminated by outgassing from the satellite, we included these effects in the calculation of the Ancillary Response File (ARF) by the “xissimarfgen” ftools task (Ishisaki et al. 2007). We then generated two different ARFs for the spectrum of each region, A^{U} and A^{B} , which respectively assumed uniform sky emission and the observed XIS image. The task wrote a value, “SOURCE_REG_RATIO”, which represents the flux ratio in the assumed spatial distribution on the sky inside the spectral accumulation region to the entire model, in the ARF file header to evaluate the flux within the region. Since the energy resolution has slowly degraded after the launch, due to radiation damage, this effect was included in the Redistribution Matrix File (RMF) by the “xismrfgen” ftools task.

We reprocessed the HXD data with the CALDB files of 2008-04-01 version, and applied data reduction by standard criteria. The HXD data was cleaned by the Earth elevation angle $> 5^\circ$, the cut-off rigidity (COR) > 6 GV, and was also processed by applying the dead-time correction. After the screening, the exposure time of the HXD data was 73.3 ks. We used the ae_hxd_pinxinode3_20070914.rsp file and ae801019010hxd_pinnxb.cl.evt as the response and the non X-ray background (NXB) files, respectively, and also simulated the 100 Ms accumulation of the cosmic X-ray background data as described in http://heasarc.gsfc.nasa.gov/docs/suzaku/analysis/pin_cxb.html using ae_hxd_pinflate3_20070914.rsp as a response file.

3. Analysis and Results

3.1. XIS spectra and the Galactic background

We extracted spectra for three regions from the optical and X-ray images as shown in figure 1 :

1. Disk component: a rectangular region of $12' \times 3'$ and $r < 6'$ circle centered on (RA, Dec) = ($1^{\text{h}}42^{\text{m}}08^{\text{s}}$, $+32^\circ32'29''$) (35.5 arcmin^2).
2. Halo component: a circular region of $r < 6'$ from the same center position of the disk component and outside the disk region (77.6 arcmin^2).
3. Background: outside of the above disk and halo region ($r > 6'$).

We first fitted the spectra of the background region and produced the extra-galactic cosmic X-ray background (CXB) and Galactic emission. This was because the O VII and O VIII lines from the Galactic emission affected these lines from NGC 4631 (see also Sato et al. 2007a). We assumed either one or two temperature *apec* model for the Galactic emission (Lumb et al. 2002), and tested the following two models: *apec* + *phabs* \times *power-law*, and *apec*₁ + *phabs* \times (*apec*₂ + *power-law*), where the *apec* models had fixed metal abundance at 1 solar with zero redshift and the absorption column for “phabs” was fixed to the Galactic value. The 0.4–5.0 keV spectra for the BI and FI sensors for all regions were fitted simultaneously, excluding an energy range of anomalous response around the Si K-edge (1.825–1.840 keV). The results of those fits

Table 1. Suzaku Observation logs for NGC 4631.

Object	Seq. No.	Obs. date	(RA, Dec)* J2000	Exp. ks	After screening (BI/FI) ks
NGC 4631	801019010	2006-11-28 03:23 – 2006-11-29 21:55	(12 ^h 42 ^m 09 ^s .3, +32°32′52″)	81.1	75.9/76.1

* Average pointing direction of the XIS, written in the RA_NOM and DEC_NOM keywords of the event FITS files.

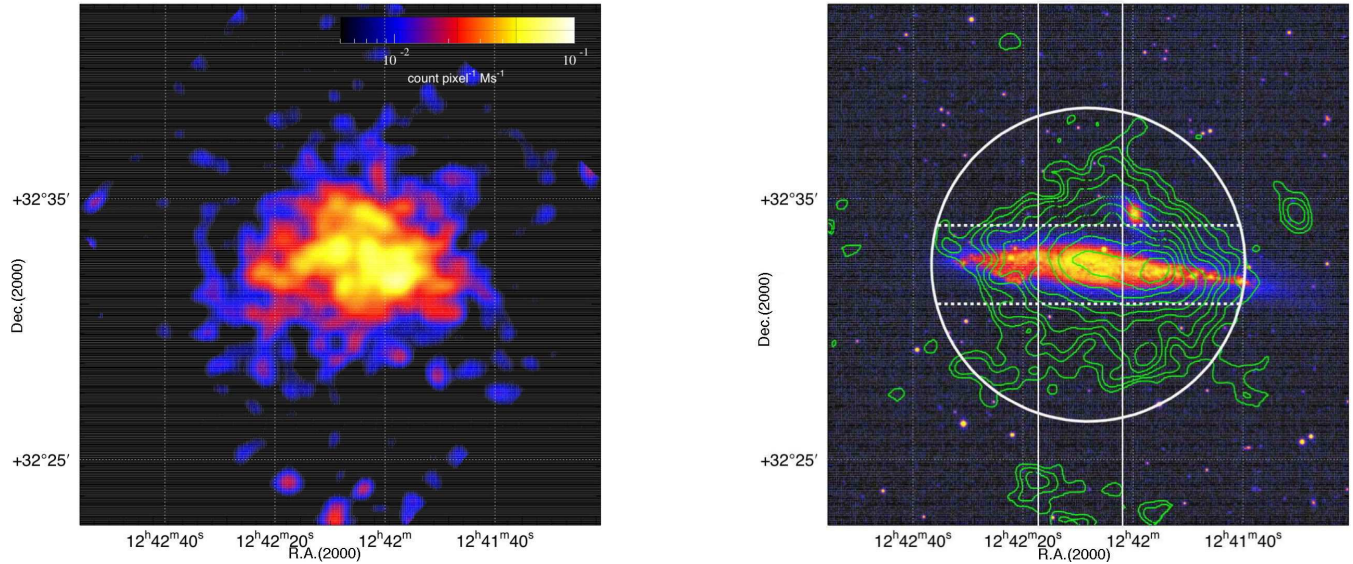


Fig. 1. Left: The X-ray image of NGC 4631 observed with Suzaku in the 0.6 – 0.7 keV energy band. Right: The X-ray contour map in linear scale from 0.5–2.0 keV overlaid on an optical image taken by DSS. For both images, the observed XIS0,1,3 images were added on the sky coordinate after removing each calibration source region, and smoothed with $\sigma = 16$ pixel or $\simeq 17''$ Gaussian. Estimated components of extragalactic X-ray background (CXB) and instrumental background (NXB) were subtracted, and the exposure was corrected, though vignetting was not corrected. The region where energy spectra were extracted are shown by solid and dotted lines in the right figure, for the halo and disk regions, respectively. Two Vertical lines show the region where we took the surface brightness profiles in section 3.2.

are given in table 2. In both cases, the surface brightness of the CXB component are consistent with the averaged value of ~ 10 photons $\text{cm}^{-2} \text{s}^{-1} \text{sr}^{-1} \text{keV}^{-1}$ at 1 keV (Gendreau et al. 1995) with fluctuations for this sky area. Afterwards, we adopted the two temperature model based on the F-test of these results. The intensity of the O VII line is 4.4 ± 0.8 photons $\text{cm}^{-2} \text{s}^{-1} \text{sr}^{-1}$ (this unit is hereafter referred to as the Line Unit or LU), which is almost the same as or slightly smaller than the previously reported values (see e.g. Sato et al. 2007b; McCammon et al. 2002). If we subtract the energy spectrum of the background from those of the halo and disk regions, the resultant line intensities without correcting the absorption effect are $17.5^{+2.2}_{-4.1}$ LU for O VII and $12.0^{+1.9}_{-1.1}$ LU for O VIII in the halo and $5.1^{+1.0}_{-1.4}$ LU for O VII and $5.8^{+0.8}_{-0.7}$ LU for O VIII in the disk region.

In order to take into account both the existence of the Galactic component itself and propagation of its statistical error, we simultaneously fitted all (BGD, halo, disk) regions with the same model: $phabs \times zphabs \times (vapec_{1\text{To}2\text{T}} + zbremss + power-law) + constant \times (apec_1 + phabs \times apec_2)$. In the model, $phabs$ corresponds to our Galactic absorption with fixed $N_{\text{H}} = 1.27 \times 10^{20} \text{cm}^{-2}$. The term $(apec_1 + phabs \times apec_2)$ represents the Galactic com-

ponent with a normalization factor to keep a uniform surface brightness. Based on the previous fits, we fixed the temperatures of the Galactic emission, $apec_1$ and $apec_2$, to be 0.114 keV and 0.310 keV, respectively, with 1 solar abundance and zero redshift. The *power-law* component which represents the CXB was set to be common for all three regions.

For the ISM emission from NGC 4631, $zphabs$ corresponds to the intrinsic absorption. The hot X-ray halo around NGC 4631 is modeled either with a one or two temperature collisionally ionized plasma with various metal abundances given by the *vapec* model. Note that the abundances were common for both temperature components, and we combined the metal abundances into five groups as O, Ne, (Mg & Al), (Si, S, Ar, & Ca), and (Fe & Ni). As we found that the continuum emission above 2 keV cannot be fitted only with the CXB, we added a *zbremss* model of $kT = 10$ keV for the low-mass X-ray binary (LMXB) component. For the spectrum of the background region, $zphabs$ and the normalizations of *vapec* and *zbremss* were all fixed to be 0.

The resultant spectra are shown in figure 2 and parameters are summarized in table 3. For the single temperature ISM model, the resultant temperatures are $kT = 0.297$ keV

Table 2. The best-fit parameters of the *apec* components for the spectra in the background region of NGC 4631 with one or two temperature models (*apec*) for Galactic emissions, and a *power-law model* for CXB.

Parameters	<i>apec</i> ₁ + <i>phabs</i> × <i>power-law</i>	<i>apec</i> ₁ + <i>phabs</i> × (<i>apec</i> ₂ + <i>power-law</i>)
kT_1 (keV)	$0.145^{+0.008}_{-0.010}$	$0.114^{+0.010}_{-0.013}$
$Norm_1^*$	0.80 ± 0.13	1.02 ± 0.42
kT_2 (keV)	–	$0.310^{+0.096}_{-0.061}$
$Norm_2^*$	–	0.13 ± 0.13
Γ	$1.68^{+0.06}_{-0.06}$	$1.58^{+0.07}_{-0.07}$
$Norm^\dagger$	0.93 ± 0.05	0.85 ± 0.09
χ^2/dof	396/375	382/373

* Normalization of the *apec* components divided by the solid angle, Ω^v , assumed in the uniform-sky ARF calculation ($20'$ radius), $Norm = \int n_e n_H dV / (4\pi(1+z)^2 D_A^2) / \Omega^v \times 10^{-20} \text{ cm}^{-5} \text{ arcmin}^{-2}$, where D_A is the angular distance to the source.

† Normalization of the *power-law* component divided by the solid angle same as the normalization of *apec*, in units of $10^{-8} \Omega^v^{-1}$ photons $\text{keV}^{-1} \text{ cm}^{-2} \text{ s}^{-1} \text{ arcmin}^{-2}$ at 1 keV.

for the disk and 0.290 keV for the halo, respectively. The emission line profiles for Si and S are difficult to distinguish, and the abundance value is almost consistent with 0. The fit statistics shown in table 3 support the two temperature model. The two temperature model gives larger absorption column and larger intrinsic luminosity than the single temperature model. The power-law index of the CXB component was obtained to be $1.48^{+0.06}_{-0.03}$, and the intensity of the LMXB component for the disk corresponds to $\sim 3 \times 10^{39} \text{ erg s}^{-1}$, which is consistent with the $L_X - M$ relation for spiral galaxies (Gilfanov 2004). A fraction of the LMXB component in the halo region is considered to be due to the extended tail of the telescope PSF. We consider that the two temperature model actually approximates multi-temperature emission, and it is represented by emission peak temperatures for O VII and O VIII with lower metal abundance. However, we do not further carry on detailed multi-temperature analysis given the statistical quality of the data.

We note possible systematic errors due to the assumption of the contamination model of the XIS. When we change the thickness of the contamination by $\pm 10\%$, the flux and the temperature of the kT_1 component of the halo changes about 30%, and 3% respectively. Thus, the abundances of metals also change by $\sim 10\%$. The kT_2 of the halo and kT_1 and kT_2 of the disk change only by 1%.

We briefly compare with the previous results for NGC 4631 here. Wang et al. (2001) reported higher temperatures (0.18 ± 0.02 and 0.61 ± 0.1 keV) and lower (0.08 ± 0.04) metal abundances after subtracting the blank field of the similar foreground absorption. Tüllmann et al. (2006) observed with XMM-Newton and detected halo emission up to 9.1 kpc from the disk. They sliced the halo into 8 regions and fitted the spectra with 2-temperature Raymond-Smith plasma model with the cosmic metal abundance. The resultant temperatures are $kT_{soft} \sim 0.17 - 0.07$ keV and $kT_{hard} \sim 0.28 - 0.2$ keV. Considering the different plasma code and assumed metal abundance, the agreement of the results is fairly good.

3.2. Hardness ratio

We produced count rate profiles in a rectangular region of $7.5 \times 42 \text{ kpc}^2$ as shown in figure 1 in two X-ray en-

ergy bands, 0.4 – 0.85 and 0.85 – 1.5 keV. With Chandra, Strickland et al. (2004) also showed surface brightness profile in 0.3 – 1 keV along the minor axis and found that an exponential model was preferred over the Gaussian or power-law models. We fitted the profile with an exponential + constant model as shown in figure 3, in which the constant component represents the sum of the X-ray and non X-ray backgrounds. The fit well represent the data, and can not be rejected within a confidence level of 95%. The constant levels are consistent within errors to the same for the north and south sides.

The obtained scale heights are summarized in table 4. These values are larger than those by Strickland et al. (2004) and could be due to the difference of the data region used in the fit. The scale height values in table 4 are consistent with each other to within 90% errors, but those in the hard band tend to be smaller than those in the soft band for both sides of the disk. This corresponds to a spectral softening, consistent with the feature obtained by the spectral fit with XMM-Newton (Tüllmann et al. 2006).

We calculated the hardness ratio for the exponential component after subtracting the constant levels with errors, and the results are plotted in figure 3. If we assume a single temperature thermal emission for the disk with abundances shown in table 3, temperatures of $kT = 0.2, 0.3,$ and 0.4 keV give HR values of 0.268, 0.610, and 0.809, respectively. Toward the outer region at > 10 kpc from the disk, kT is consistent with > 0.2 keV. The small or no decline of the temperature may imply that the gas is adiabatically expanding into a vacuum with small mechanical work.

3.3. Search for the hard X-ray emission

Since NGC 4631 is accompanied by a strong radio halo which is likely to be due to synchrotron emission by relativistic electrons, one can expect inverse Compton emission in the hard X-ray band. We searched for hard X-ray emission with the PIN detector of the HXD over the $34'$ fov. After subtraction of the NXB component estimated by the standard modeling method in the current processing, the energy spectrum was consistent with the expected CXB level. Due to the current uncertainty of the NXB

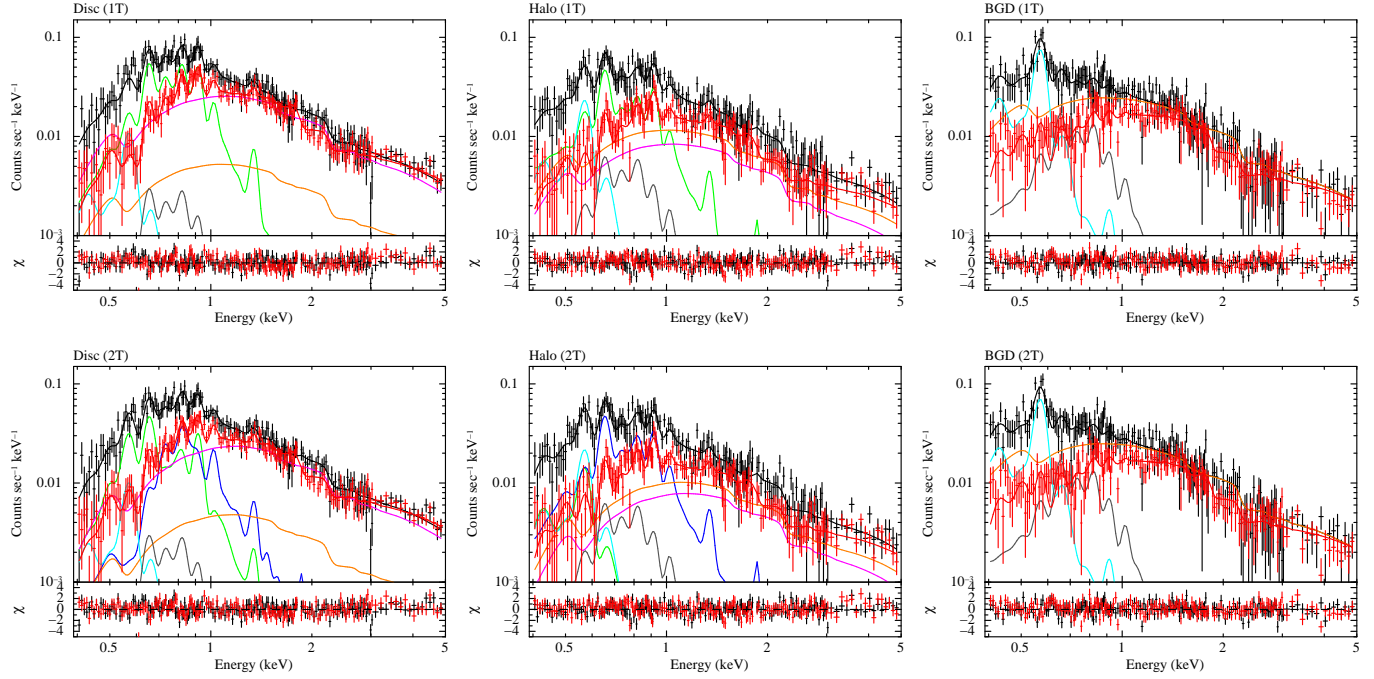


Fig. 2. The panels show the observed spectra after subtracting the NXB component for all regions of NGC 4631 which are denoted in the panels, and they are plotted by black and red crosses for BI and FI, respectively. The spectra not corrected for the integrated area. They are fitted with the model: $phabs \times zphabs \times (vapec_{1\text{Tor}2\text{T}} + zbremss + power-law) + constant \times (apec_1 + phabs \times apec_2)$ as shown by black and red lines for the BI and FI spectra. For simplicity, only the model components for BI spectra are shown. Green and blue lines are the ISM component by *vapec*, cyan and grey are the Galactic background emission by *apec*₁ and *apec*₂, magenta and orange are the LMXB and CXB component, respectively. The lower panels show the fit residuals in unit of σ .

Table 3. Summary of the best-fit parameters of one or two *vapec* components by simultaneous fit of all regions.

	ISM 1T		ISM 2T	
	Disk	Halo	Disk	Halo
kT_1 (keV)	$0.297^{+0.009}_{-0.016}$	$0.290^{+0.027}_{-0.053}$	$0.209^{+0.025}_{-0.016}$	$0.096^{+0.065}_{-0.015}$
$Norm_1^*$	$4.5^{+2.4}_{-2.2}$	$0.9^{+1.2}_{-0.8}$	$8.0^{+2.3}_{-4.5}$	$4.5^{+13.4}_{-4.2}$
$flux_1^\dagger$ (erg cm ⁻² s ⁻¹)	2.2×10^{-13}	1.3×10^{-13}	1.6×10^{-13}	2.3×10^{-14}
kT_2 (keV)	–	–	$0.480^{+0.073}_{-0.101}$	$0.300^{+0.016}_{-0.027}$
$Norm_2^*$	–	–	$2.3^{+1.7}_{-1.3}$	$2.2^{+2.2}_{-1.3}$
$flux_2^\dagger$ (erg cm ⁻² s ⁻¹)	–	–	1.1×10^{-13}	1.4×10^{-13}
O (solar)	$0.97^{+0.81}_{-0.55}$	$1.34^{+1.06}_{-0.91}$	$0.73^{+0.69}_{-0.38}$	$0.81^{+0.55}_{-0.43}$
Ne (solar)	$1.92^{+1.70}_{-1.25}$	$2.18^{+5.34}_{-1.37}$	$1.60^{+2.11}_{-0.72}$	$1.09^{+1.14}_{-0.55}$
Mg, Al (solar)	$1.85^{+3.41}_{-1.01}$	$2.29^{+14.06}_{-1.79}$	$1.26^{+0.70}_{-0.65}$	$0.98^{+1.14}_{-0.69}$
Si, S, Ar, Ca (solar)	$0.45^{+2.55}_{-0.45}$	$5.98^{+20.57}_{-4.80}$	$0.60^{+2.65}_{-0.60}$	$2.17^{+0.83}_{-2.17}$
Fe, Ni(solar)	$1.09^{+0.75}_{-0.64}$	$0.85^{+1.47}_{-0.63}$	$0.93^{+0.64}_{-0.41}$	$0.46^{+0.31}_{-0.23}$
extra absorption (cm ⁻²)	$3.4^{+4.0}_{-2.0} \times 10^{20}$	$0.0^{+4.6}_{-0.0} \times 10^{20}$	$8.6^{+4.4}_{-4.0} \times 10^{20}$	$6.4^{+4.4}_{-5.7} \times 10^{20}$
LMXB flux † (erg cm ⁻² s ⁻¹)	3.0×10^{-13}	8.5×10^{-14}	2.6×10^{-13}	7.8×10^{-14}
Hot gas luminosity ‡ (erg s ⁻¹)	1.9×10^{39}	0.9×10^{39}	3.1×10^{39}	1.6×10^{39}
χ^2/dof	1198/1114		1172/1109	

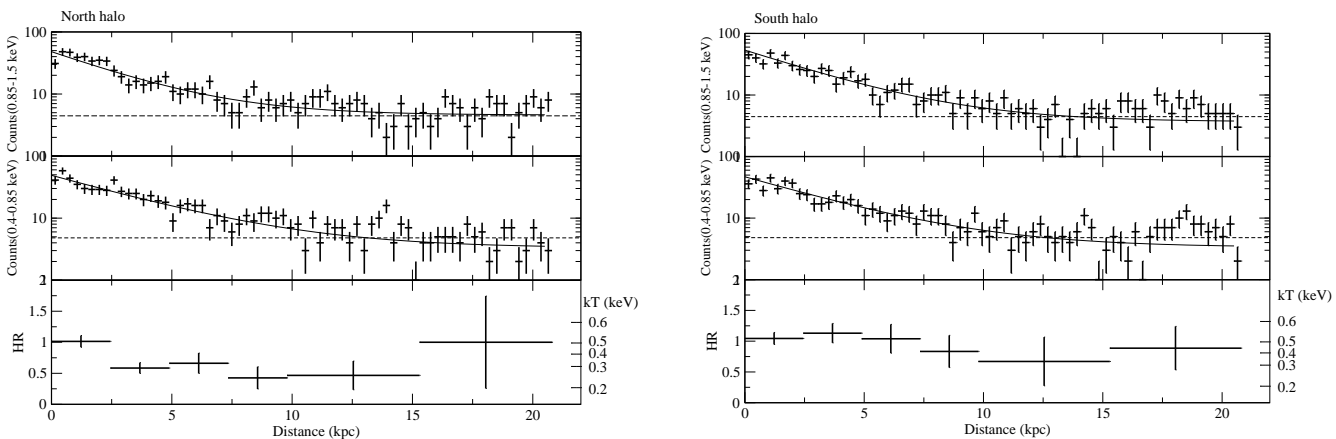
* Normalization of the *vapec* component scaled with a factor of $SOURCE_RATIO_REG / AREA$, which is $Norm = \frac{SOURCE_RATIO_REG}{AREA} \int n_e n_H dV / [4\pi (1+z)^2 D_A^2] \times 10^{-20} \text{ cm}^{-5} \text{ arcmin}^{-2}$, where D_A is the angular distance to the source.

† Flux within the accumulated region between 0.5 and 2 keV

‡ Intrinsic luminosity between 0.5 and 2 keV

Table 4. Scale height of the X-ray emission

Scale height (kpc)		North side	South side
Hard band	(0.85 – 1.5 keV)	3.01 ± 0.47	3.33 ± 0.47
	(χ^2/dof)	(66.02/65)	(81.30/65)
Soft band	(0.40 – 0.85 keV)	3.85 ± 0.58	3.72 ± 0.59
	(χ^2/dof)	(79.24/65)	(87.08/65)

**Fig. 3.** Count rate profile of hard (0.85 – 1.5 keV) and soft (0.4 – 0.85 keV) X-ray bands without subtracting background and the hardness ratio in the north (left) and the south (right) side. The region is shown in figure 1. Dashed lines in the count rate profile are drawn to show the averaged rate taken from the background region for the spectral fitting.

estimation, we scaled the normalization of the NXB by -3% (Kokubun et al. 2007), and the spectrum was fitted by $phabs \times power-law$ model with a fixed photon index to be 2.0 in 12–60 keV.

The resultant upper limit corresponding to 1σ level of the flux was 5.5×10^{-12} erg cm^{-2} s^{-1} in 12–60 keV, with the estimated contribution from LMXBs with an energy spectrum of $kT = 10$ keV is 4×10^{-13} erg cm^{-2} s^{-1} . The Very Large Array (VLA) observations at 1.49 GHz indicated a radio halo of NGC 4631 with a brightness of about 1.22 Jy (Hummel & Dettmar 1990). If we assume an inverse Compton process with 2.7 K photons scattered by the same relativistic electrons responsible for the radio halo, the strength of the magnetic field is constrained. Following the prescription given by Harris & Grindlay (1979), we derived the lower limit of the magnetic field strength to be $B > 0.5 \mu\text{G}$, which is consistent with the previous estimation of $5 \mu\text{G}$ from the polarized component of the radio emission (Hummel et al. 1991).

4. Discussion

Suzaku observations of NGC 4631 showed significant emission lines from an extended halo region, including those from O for the first time. We examined an abundance pattern for the X-ray halo in the form of the number ratio to O as shown in figure 4. To make this plot, Z/O ratios are determined by two parameter errors from the simultaneous fit of all regions as described in section 3.1. In this plot, the SN Ia yields were taken from W7

model in Iwamoto et al. (1999). For SN II, Nomoto et al. (2006) gave an average yields for the Salpeter’s IMF of stellar masses from 10 to $50 M_{\odot}$ with the progenitor metallicity of $Z = 0.02$. If the metallicity of progenitors increases to $Z = 1$, relative abundances of ejecta increase by at most 20% for Fe/O. Also the solar abundance template of Anders & Grevesse (1989), and the average abundance pattern for 4 clusters and groups (Sato et al. 2007a) are plotted together. The pattern in clusters is well fitted by a combination of SN Ia and SN II with a ratio of 1:3.5. The metal abundance of NGC 4631 halo disagrees with that of SN Ia and the cluster average, but is consistent with the SN II yields. In the disk component, Fe shows relatively higher abundance and the abundance pattern is consistent with the Solar abundance given by Anders & Grevesse (1989).

For the study of the energetics of the gas, we estimate the density, mass, and total energy of the X-ray emitting gas. As shown in figure 3, the X-ray profile of the halo is very smooth, and there is no boundary recognized between the disk and the halo. Hereafter, we will not discriminate the disk and the halo component and treat them at the same time. We assume a simple exponential model of $n(z) = n_0 \times \exp(-z/h)$ with z indicating the distance from the galactic plane, within a radius of 10 kpc for the coronal gas. Since the scale height of the surface brightness is about 3.5 kpc as shown in Table 4, we can adopt the density scale height to be $h = 7$ kpc. A single temperature model gave us a lower limit of the density at the disk as

$n_0 = 2 \times 10^{-3} \text{ cm}^{-3}$, and the pressure as $n_0 T = 7 \times 10^3 \text{ cm}^{-3} \text{ K}$, which are consistent with the previous values by Wang et al. (1995); Wang et al. (2001). With this density, the total mass of the X-ray emitting gas is $1.3 \times 10^8 M_\odot$, and the stored thermal energy is $2 \times 10^{56} \text{ erg}$. Assuming an O abundance of 0.8 solar, the O mass in the hot gas in both the disk and the halo is $\sim 10^6 M_\odot$.

Since the cooling time in the disk is about $\sim 6 \times 10^8 \text{ yr}$ assuming the cooling function of Sutherland & Dopita (1993), the required energy input rate is $3 \times 10^{47} \text{ erg yr}^{-1}$ and a mass transfer rate of $\sim 0.2 M_\odot \text{ yr}^{-1}$, respectively. If one employs a flow time to a radius of 10 kpc, it is about $5 \times 10^7 \text{ yr}$ and 10 times higher rates for energy input and mass transfer are implied. Wang et al. (1995) estimated the maximum mass flow rate from the density multiplied by the sound velocity to be $1.4 M_\odot \text{ yr}^{-1}$. Based on the UV observation of O VI line, Otte et al. (2003) estimated the flow rate to be $0.48 \sim 2.8 M_\odot \text{ yr}^{-1}$ assuming a cooling flow model by Edgar & Chevalier (1986). Considering the differences in the assumed physical process and condition, mass flow rates are in good agreement around an approximate value of $1 M_\odot \text{ yr}^{-1}$.

The most likely source of the energy and the material in the coronal gas is SNe. The SFR is estimated by the FIR luminosity as $3 M_\odot \text{ yr}^{-1}$ (Strickland et al. 2004). As NGC 4631 has an edge-on morphology, the emission could be underestimated due to absorption through the disk. Persic et al. (2004) proposed another method to estimate the SFR using the X-ray luminosity of high mass X-ray binaries (HMXB) in the 2–10 keV band. A typical luminosity ratio of HMXB/LMXB of 0.2 gives a SFR of $1.2 M_\odot \text{ yr}^{-1}$. If we assume that all the flux above 2 keV comes from HMXBs, it gives an upper limit as $6 M_\odot \text{ yr}^{-1}$. We note that a spectral fit with a power-law component with $\Gamma = 1.2$ as suggested by Persic et al. (2004) requires a steep $\Gamma = 1.55$ CXB component. The two independent estimates give a consistent SFR of $\sim 3 M_\odot \text{ yr}^{-1}$, which is almost the same as or a little less than the level in our Galaxy, i.e. $\sim 5 M_\odot \text{ yr}^{-1}$ (Zinnecker & Yorke 2007). Assuming the Salpeter’s IMF integrated over 0.1 to $50 M_\odot$, a SFR of $3 M_\odot \text{ yr}^{-1}$ gives a SN II rate of $7 \times 10^{-3} \text{ SN yr}^{-1}$. In addition to SN II, SN Ia of $2.5 \times 10^{-3} \text{ SN yr}^{-1}$ is expected for the total mass of $2.6 \times 10^{10} M_\odot$ and the SFR of $3 M_\odot \text{ yr}^{-1}$ (Sullivan et al. 2006).

If SNe are the source of the energy and the mass of the halo gas estimated above, one SN needs to supply an energy of $3 \times 10^{49} \text{ erg}$ and a mass of $\sim 20 M_\odot$ including an O mass of $0.2 M_\odot$. Therefore, 3% of the typical explosion energy of 10^{51} erg and $20 M_\odot$ from the ejecta and ambient material have to escape into the halo. These values indicate that the halo gas is produced very efficiently. Since one SN produces 0.14 and $1.8 M_\odot$ of O for SN Ia and SN II, respectively (Iwamoto et al. 1999), a supply of $0.2 M_\odot$ of O seems plausible. The abundance pattern in the halo is, however, well represented by the SN II products, although the above estimated rate between SN Ia and SN II is $\sim 1 : 3$. It may imply the selective escape of SN II ejecta into the halo gas, which can result if the occurrence of SN II is concentrated in the starforming region. In

this case, superbubbles are formed and the metal-rich hot gas escapes along a chimney to the halo space (Norman & Ikeuchi 1989).

We must note two possibilities which may bias the abundance and temperature estimate. Lallement (2004) pointed out the possible contribution of charge exchange (CX) processes between the galactic wind and gas clouds in the halo. The CX spectrum is dominated by emission lines, and it tends to decrease the apparent temperature of the halo, kT_1 in table 3. The process was seriously evaluated for the M82 halo (Ranalli et al. 2008) and M82 “cap” region (Tsuru et al. 2007), and they found that almost all of the O VII triplet could be produced by CX. In the case of NGC 4631, a dust arch with a mass of a few $10^8 M_\odot$ was discovered in the halo, but there seemed to be no connection between the X-ray emission and the dust arch (Taylor & Wang 2003). Thus, the contribution from CX might not be so large, considering the low velocity of the outflow and the low density of the neutral material, which is also suggested by the slow decline of the X-ray temperature. We must wait for improved spectroscopic observation to distinguish the physical process of the emission.

Another possibility is the role of dust. Dust of silicates (Mg_2SiO_4) and other forms with a mass of $\sim 5 M_\odot \text{ SN}^{-1}$ can be formed 300–600 days after SN II explosions (Todini & Ferrara 2001). Since it requires more than 10^7 yr to evaporate in the low-density environment with $n = 10^{-3} \text{ cm}^{-3}$ (Tielens et al. 1994), a significant amount of metals may be held in dust. We hope that future high resolution X-ray spectroscopy will be able to show the ionization condition of plasmas in the galactic winds more precisely.

5. Conclusion

We determined the temperature and metal abundance of the X-ray emitting halo gas around NGC 4631. The total energy, mass, and metals in the halo can be supplied by SNe with the currently estimated SFR, if the outflow efficiently carries metal-rich gas from the starforming regions into the halo. The effect of neutral material and dust should be taken into account to understand the plasma properties in the halo.

Acknowledgement

The authors acknowledge Dr. Tai Oshima for his information about detailed Chandra data analysis and support for the observation. Part of this work was financially supported by the Ministry of Education, Culture, Sports, Science and Technology of Japan, Grant-in-Aid for Scientific Research No. 20340041, 20340068 and 19840043.

The Digitized Sky Survey was produced at the Space Telescope Science Institute under U.S. Government grant NAG W-2166. This research has made use of the NASA/IPAC Extragalactic Database (NED) which is operated by the JPL, under contract with NASA.

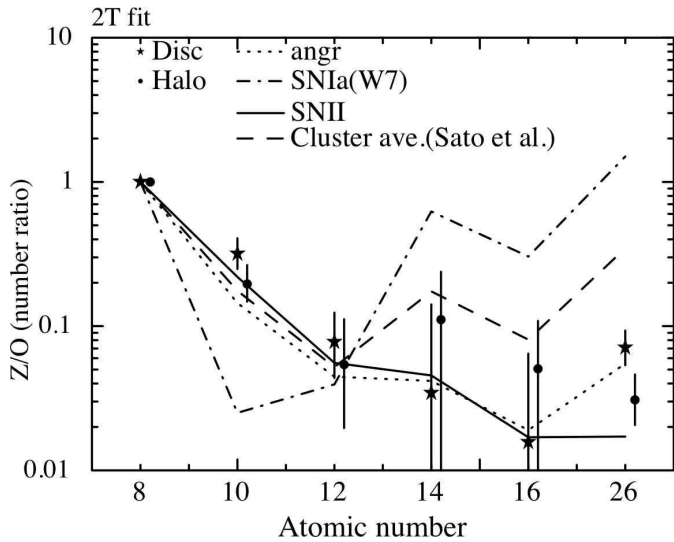


Fig. 4. Number ratios of Ne, Mg, Si, S, and Fe to O for disk and halo regions. Solid, dotted, dashed, and dot-dashed lines correspond to the number ratios of metals to O for abundance patterns of SNe II yield of Nomoto et al. (2006), solar abundance by Anders & Grevesse (1989), cluster average in Sato et al. (2007a), and SNe Ia yield of Iwamoto et al. (1999), respectively.

Ranalli, P., Comastri, A., Origlia, L., & Maiolino, R. 2008, *MNRAS*, 386, 1464
 Read, A. M., & Stevens, I. R. 2002, *MNRAS*, 335, L36
 Sato, K., Tokoi, K., Matsushita, K., Ishisaki, Y., Yamasaki, N. Y., Ishida, M., & Ohashi, T. 2007, *ApJL*, 667, L41
 Sato, K., et al. 2007, *PASJ*, 59, 299
 Strickland, D. K., Heckman, T. M., Colbert, E. J. M., Hoopes, C. G., Weaver, K. A. 2004, *ApJS*, 151, 193
 Sullivan, M., et al. 2006, *ApJ*, 648, 868
 Sutherland, R. S., & Dopita, M. A. 1993, *ApJS*, 88, 253
 Tawa, N., et al. 2008, *PASJ*, 60, S22
 Taylor, C. L., & Wang, Q. D. 2003, *AJ*, 125, 1204
 Tielens, A. G. G. M., McKee, C. F., Seab, C. G., & Hollenbach, D. J. 1994, *ApJ*, 431, 321
 Todini, P., & Ferrara, A. 2001, *MNRAS*, 325, 726
 Tsuru, T. G., et al. 2007, *PASJ*, 59, S269
 Tüllmann, R., Pietsch, W., Rossa, J., Breitschwerdt, D., Dettmar, R.-J. 2006, *A&A*, 448, 43
 Veilleux, S., Cecil, G., & Bland-Hawthorn, J. 2005, *ARAA*, 43, 769
 Wang, Q. D., Walterbos, R. A. M., Steakley, M. F., Norman, C. A., & Braun, R. 1995, *ApJ*, 439, 176
 Wang, Q. D., Immler, S., Walterbos, R., Lauroesch, J. T., & Breitschwerdt, D. 2001, *ApJL*, 555, L99
 Zinnecker, H., & Yorke, H. W. 2007, *ARA&A*, 45, 481

References

Anders, E., & Grevesse, N. 1989, *Geochim. Cosmochim. Acta*, 53, 197
 Bauer, M., Pietsch, W., Trinchieri, G., Breitschwerdt, D., Ehle, M., & Read, A. 2007, *A&A*, 467, 979
 Dickey, J. M., & Lockman, F. J. 1990, *ARA&A*, 28, 215
 Edgar, R. J., & Chevalier, R. A. 1986, *ApJL*, 310, L27
 Gendreau, K. C., et al. 1995, *PASJ*, 47, L5
 Gilfanov, M. 2004, *MNRAS*, 349, 146
 Golla, G. & Hummel, E. 1994, *A&A*, 284, 777
 Golla, G. & Wielebinski, R. 1994, *A&A*, 286, 733
 Harris, D. E., & Grindlay, J. E. 1979, *MNRAS*, 188, 25
 Hummel, E., & Dettmar, R.-J. 1990, *A&A*, 236, 33
 Hummel, E., Beck, R., & Dahlem, M. 1991, *A&A*, 248, 23
 Ishisaki, Y., et al. 2007, *PASJ*, 59, S113
 Iwamoto, K., Brachwitz, F., Nomoto, K., Kishimoto, N., Umeda, H., Hix, W. R., & Thielemann, F.-K. 1999, *ApJS*, 125, 439
 Kokubun, M., et al. 2007, *PASJ*, 59, S35
 Koyama, K., et al. 2007, *PASJ*, 59, S23
 Lallement, R. 2004, *A&A*, 422, 391
 Lumb, D. H., Warwick, R. S., Page, M., & De Luca, A. 2002, *A&A*, 389, 93
 McCammon, D., et al. 2002, *ApJ*, 576, 188
 Mitsuda, K., et al. 2007, *PASJ*, 59, S1
 Nomoto, K., Tominaga, N., Umeda, H., Kobayashi, C., & Maeda, K. 2006, *Nuclear Physics A*, 777, 424
 Norman, C. A., & Ikeuchi, S. 1989, *ApJ*, 345, 372
 Oshima, T. 2003, Ph.D. thesis, University of Tokyo
 Otte, B., Murphy, E. M., Howk, J. C., Wang, Q. D., Oegerle, W. R., & Sembach, K. R. 2003, *ApJ*, 592, 826
 Persic, M., Rephaeli, Y., Braitto, V., Cappi, M., Della Ceca, R., Franceschini, A., Gruber, D. E. 2004, *A&A*, 419, 849
 Pietsch, W., et al. 2001, *A&A*, 365, L174